

Monolayer Topological Insulators: Silicene, Germanene and Stanene

Motohiko Ezawa

Department of Applied Physics, University of Tokyo, Hongo 7-3-1, 113-8656, Japan

We report the recent progress on the theoretical aspects of monolayer topological insulators including silicene, germanene and stanene, which are monolayer honeycomb structures of silicon, germanium and tin, respectively. They show quantum spin Hall effects in nature due to the spin orbit interaction. The band gap can be tuned by applying perpendicular electric field, which induces a topological phase transition. We also analyze the topological properties of generic honeycomb systems together with the classification of topological insulators. Phase diagram of topological insulators and superconductors in honeycomb systems are explicitly determined. We also investigate topological electronics including a topological field-effect transistor, the topological Kirchhoff's law and the topological spin-valleytronics.

I. INTRODUCTION

Monolayer materials are one of the most active fields of condensed matter physics. Graphene, monolayer honeycomb structure of carbon atoms, is the first experimentally realized monolayer material. Its low-energy band structure is described by the Dirac theory, which results in various novel physical properties¹⁻⁵. The success of graphene evokes an extensive search for other monolayer materials. In particular, monolayer topological materials are fascinating, realizing topological insulators and topological superconductors.

A natural question is whether other monolayer honeycomb systems purely made of one kind of atoms are possible. It is shown that monolayer honeycomb systems made of silicon, germanium and tin are possible, which are named silicene, germanene and stanene, respectively. Silicene is named after the combination of silicon and suffix "ene", which means the sp_2 bonding structure⁶. Germanene is also named after germanium + "ene". Stanene is named after the Latin word "stannum" for tin⁷.

Silicene, Germanene and stanene are expected to be topological insulators. Topological insulator (TI) is a distinctive state of matter indexed by topological numbers, and characterized by an insulating gap in the bulk accompanied by topologically protected gapless edges^{8,9}. Thus the physics of these materials is located at the confluence of graphene and topological insulators, which results in very rich physics.

Silicene and germanene are proposed by first-principles calculations^{6,10-12}, where their stability and the emergence of the Dirac cone are predicted by first-principles calculations. It is shown that the band gap of silicene is electrically controllable by applying perpendicular electric field to silicene plane by the first-principle calculations^{13,14} and based on the Dirac theory¹⁵. A first-principles calculation shows that the Dirac cones are hidden in silicene fabricated on the Ag substrate due to the strong hybridization between silicene and Ag substrate¹⁶.

First suggestive observations¹⁷⁻¹⁹ of silicene were reported in 2010. Silicene has been grown on various substrates such as the Ag substrate²⁰⁻²² and the ZrB_2 substrate²³, the Ir substrate²⁴ and the MoS_2 substrate²⁵. Germanene is synthesized on the Au substrate²⁶ and Pt substrate²⁷. There are several experiments on silicene²⁸⁻³². In particular, silicene was demonstrated in 2015 to act as a field-effect transistor at room

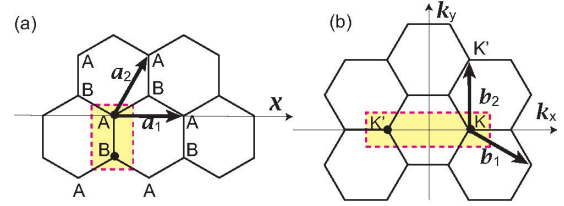


FIG. 1: (a) The honeycomb structure, made of two fundamental vectors \mathbf{a}_1 and \mathbf{a}_2 , consists of two sublattices made of A and B sites. A dotted rectangular represents a unit cell. (b) The reciprocal lattice is also a honeycomb lattice. A dotted rectangular represents a unit cell, which contains two inequivalent points K and K' .

temperature³³. There are reviews on experimental aspects of silicene³⁴⁻³⁶.

There are several proposals on realizing free-standing like silicene on substrates by first-principles calculations. Silicene will be grown on graphene³⁷, hexagonal boron-nitride³⁸, hydrogen-processed Si(111) surface¹⁶, hydrogen-processed Ge(111) surface³⁹, Cl-passivated Si(111) and clean $CaF_2(111)$ surfaces⁴⁰, solid argon⁴¹, between bilayer graphene⁴² and intercalating alkali metal atoms between silicene and the metal substrates⁴³.

II. GRAPHENE AND SILICENE

The basic structure of graphene and silicene is a honeycomb lattice generated by the fundamental translational vectors \mathbf{a}_1 and \mathbf{a}_2 . It consists of two triangular sublattices made of inequivalent lattice sites A and B [Fig.1(a)]. The reciprocal lattice is also a honeycomb lattice in the momentum space [Fig.1(b)], which constitutes the Brillouin zone.

A. Graphene

Graphene is described by the simplest tight-binding model on a honeycomb lattice [Fig.2],

$$\hat{H}_0 = -t \sum_{\langle i,j \rangle} c_{is}^\dagger c_{js}, \quad (2.1)$$

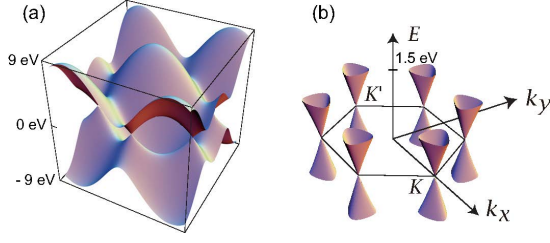


FIG. 2: Band structure of graphene. (a) Six valleys are seen in this figure. (b) The gap is closed at the K and K' points, where the band structure looks like a cone. It is called the Dirac cone because the dispersion is linear. Among six cones only two are physically inequivalent.

where c_{is}^\dagger creates an electron with spin polarization $s = \uparrow\downarrow$ at site i , $\langle i, j \rangle$ runs over all the nearest neighbor hopping sites, and t is the transfer energy. By diagonalizing the Hamiltonian we obtain the band structure, which we illustrate in Fig.2(a). It consists of valleys or cones near the Fermi surface. The cones touch the Fermi surface at two inequivalent points, that is, the K and K' points in the Brillouin zone [Fig.2(b)].

We are interested in physics near the Fermi energy. To derive the relevant Hamiltonian, we rewrite (2.1) as

$$\hat{H}_0 = t \sum_s \int d^2k' \begin{pmatrix} c_{As}^\dagger & c_{Bs}^\dagger \end{pmatrix} \begin{pmatrix} 0 & f(\mathbf{k}) \\ f^*(\mathbf{k}) & 0 \end{pmatrix} \begin{pmatrix} c_{As} \\ c_{Bs} \end{pmatrix} \quad (2.2)$$

in the momentum space, with

$$f(\mathbf{k}) = e^{-iak_y/\sqrt{3}} + 2e^{iak_y/2\sqrt{3}} \cos \frac{ak_x}{2}. \quad (2.3)$$

The energy spectrum is obtained as

$$E(\mathbf{k}) = t \sqrt{1 + 4 \cos \frac{ak_x}{2} \cos \frac{\sqrt{3}ak_y}{2} + 4 \cos^2 \frac{ak_x}{2}}. \quad (2.4)$$

The gap closes at the K_η point defined by

$$K_\eta = \frac{1}{a} \left(\eta \frac{4\pi}{3}, 0 \right) \quad \text{with} \quad \eta = \pm. \quad (2.5)$$

The K_+ and K_- points are identical to the K and K' points, respectively. Because the dispersion relation is linear for $k_i \simeq 0$, they are also called the Dirac points: See Figs.2 and 3(a2).

In the vicinity of the K_η point, the Hamiltonian is approximated by

$$\hat{H}_\eta = \sum_s \int d^2k (c_{As}^\dagger, c_{Bs}^\dagger) H_{s_z}^\eta \begin{pmatrix} c_{As}^\eta \\ c_{Bs}^\eta \end{pmatrix}, \quad (2.6)$$

with

$$H_\eta^s = \hbar v_F (\eta k_x \tau_x + k_y \tau_y) = \hbar v_F \begin{pmatrix} 0 & \eta k_x - ik_y \\ \eta k_x + ik_y & 0 \end{pmatrix}, \quad (2.7)$$

where $\boldsymbol{\tau} = (\tau_x, \tau_y, \tau_z)$ is the Pauli matrix of the sublattice pseudospin for the A and B sites, and $v_F = \frac{\sqrt{3}}{2\hbar} at$ is the Fermi velocity with a being the lattice constant. The dispersion relation is linear for $k_i \simeq 0$. We refer to H_η^s as the Dirac Hamiltonian at the Dirac point K_η .

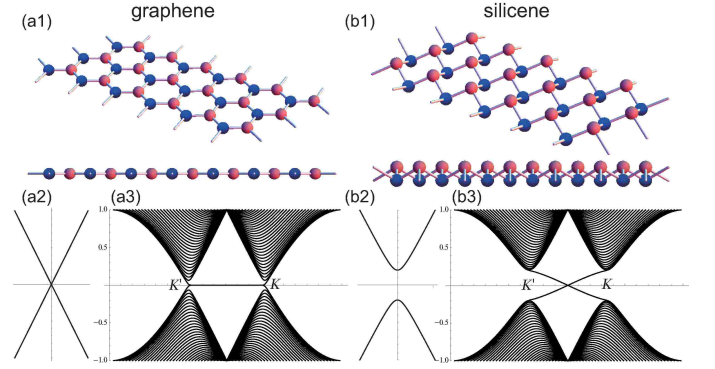


FIG. 3: (a1) The lattice structure of graphene is planar, but (b1) that of silicene is buckled. Red and blue balls represent A and B sites. (a2) The band gap of graphene is closed, where the dispersion is linear near the Fermi energy. (b2) The band gap of silicene is open. (a3) A flat line connecting the K and K' points represents gapless flat edge modes in a nanoribbon. It contains 4-fold degenerate edge states for up/down-spin and left/right movers. (b3) Two lines connecting the tips of the Dirac cones represents gapless edge modes of a nanoribbon. Each line contains 2-fold degenerate edge states.

B. Silicene and tunable band gap

The basic nature of silicene is described also by the tight-binding model (2.1). There are two additional features making silicene essentially different from graphene. One is the presence of the spin-orbit interaction, which makes silicene a topological insulator⁴⁴. The other is its buckled structure with a layer separation between the two sublattices [Fig.3(b1)]. This freedom allows us to tune the gap by introducing a potential difference between the two sublattices^{13–15}. When we apply electric field E_z perpendicular to silicene, the tight-binding Hamiltonian reads

$$\begin{aligned} \hat{H} = & -t \sum_{\langle i,j \rangle s} c_{is}^\dagger c_{js} + i \frac{\lambda_{SO}}{3\sqrt{3}} \sum_{\langle\langle i,j \rangle\rangle s} s \nu_{ij} c_{is}^\dagger c_{js} \\ & - \ell \sum_{is} \mu_i E_z c_{is}^\dagger c_{is}, \end{aligned} \quad (2.8)$$

where $\langle\langle i, j \rangle\rangle$ run over all the next-nearest neighbor hopping sites. The spin index stands for $s = \uparrow\downarrow$ for indices and for $s = \pm$ within equations. It describes germanene and stanene as well.

We explain each term. (i) The first term represents the usual nearest-neighbor hopping with the transfer energy t . (ii) The second term represents the effective SO coupling with λ_{SO} , where $\nu_{ij} = +1$ if the next-nearest-neighboring hopping is anticlockwise and $\nu_{ij} = -1$ if it is clockwise with respect to the positive z axis⁴⁵. (iii) The third term represents the staggered sublattice potential with $\mu_i = +1$ (-1) for the A (B) site¹⁵. Explicit values of these parameters are summarized in the Table I. By diagonalizing the Hamiltonian by setting $E_z = 0$, we obtain the band structure illustrate as in Fig.3(b2). The prominent feature is that the gap is open due to the SO interaction, and hence silicene is an insulator. A large SO interaction with $\lambda_{SO} = 0.3\text{eV}$ is materialized in functionalized

	$t(\text{eV})$	v	$a(\text{\AA})$	λ_{SO}	λ_{R}	ℓ	θ
Graphene	2.8	9.8	2.46	10^{-3}	0	0	90
Silicene	1.6	5.5	3.86	3.9	0.7	0.23	101.7
Germanene	1.3	4.6	4.02	43	10.7	0.33	106.5
Stanene	1.3	4.9	4.70	43	9.5	0.33	107.1

TABLE I: The parameters charactering graphene, silicene and germanene. Here, v_F is in the unit of 10^5 m/s , and λ_{SO} in the unit of meV. λ_{R} is the Rashba SO interaction strength in the unit of meV: See (7.1). ℓ is the buckle height, while θ is the bond angle. Taken from Ref.⁴⁶.

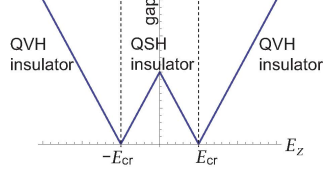


FIG. 4: Electrically tunable band gap and topological phase transition of silicene. Silicene is a QSH insulator without electric field. By applying electric field, the band gap reduces and closes at the critical electric field $\pm E_{\text{cr}}$. Above the critical electric field, silicene becomes a QVH insulator.

stanene⁷, which will be a topological insulator at room temperature.

The low-energy physic near the Fermi energy is described by the Dirac theory, which is constructed just as in the case of graphene. We rewrite the Hamiltonian (2.8) in the form of (2.6). The Dirac Hamiltonian is explicitly given by

$$H_s^\eta = \begin{pmatrix} \Delta_s^\eta & \hbar v_F(\eta k_x - i k_y) \\ \hbar v_F(\eta k_x + i k_y) & -\Delta_s^\eta \end{pmatrix}, \quad (2.9)$$

where

$$\Delta_s^\eta = \eta s \lambda_{\text{SO}} - \ell E_z \equiv -\ell(E_z - \eta s E_{\text{cr}}), \quad (2.10)$$

with

$$E_{\text{cr}} \equiv \lambda_{\text{SO}}/\ell. \quad (2.11)$$

Note that Δ_s^η acts as the Dirac mass. The energy spectrum reads

$$E(\mathbf{k}) = \pm \sqrt{(\hbar v_F k)^2 + (\Delta_s^\eta)^2}. \quad (2.12)$$

The gap is given by $2|\Delta_s^\eta| = 2\ell|E_z - \eta s E_{\text{cr}}|$.

It is important that the band gap is tunable by controlling external electric field E_z . The gap is open when $E_z = 0$. As $|E_z|$ increases, the gap become narrower [Fig.4], and it closes at $E_z = \eta s E_{\text{cr}}$, where silicene is semimetallic just as in graphene. As $|E_z|$ increases further, the gap opens again.

C. Generalized Dirac mass terms

There are actually other ways to control the band gap by introducing other interactions to silicene. Since each Dirac

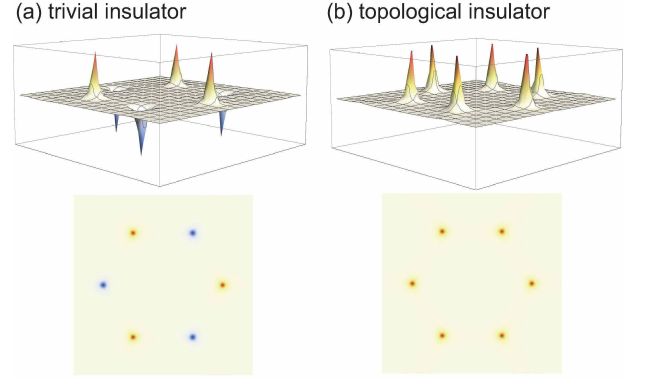


FIG. 5: Berry curvature in (a) the trivial insulator and (b) the topological insulator. It is strictly localized in the vicinity of the K and K' points. The Chern number, the integration of the Berry curvature over the Brillouin zone, is zero for a trivial insulator, while it is non-zero for a topological insulator.

cone is indexed by two parameters $\eta = \pm$ and $s = \pm$, the most general Dirac mass must have the following expression,

$$\Delta_s^\eta = \eta s \lambda_{\text{SO}} - \lambda_V + \eta \lambda_H + s \lambda_{SX}, \quad (2.13)$$

so that it has four independent parameters, λ_{SO} , λ_V , λ_H and λ_{SX} . We have already discussed the first two terms representing the SO interaction and the sublattice staggered potential with $\lambda_V = \ell E_z$. We may write down the tight-binding terms that yield the fourth and fifth terms⁴⁷,

$$i \frac{\lambda_H}{3\sqrt{3}} \sum_{\langle\langle i,j \rangle\rangle s} \nu_{ij} c_{is}^\dagger c_{js}, \quad \lambda_{SX} \sum_{is} s \mu_i c_{is}^\dagger c_{is}. \quad (2.14)$$

The fourth term describes the Haldane interaction induced by the photo-irradiation, where $\lambda_\Omega = \hbar v_F^2 \mathcal{A}^2 \Omega^{-1}$ with Ω the frequency and \mathcal{A} the dimensionless intensity⁴⁸⁻⁵⁰. The fifth term describes the antiferromagnetic exchange magnetization⁴⁷.

Here we note that there are a variety of 2D materials whose low-energy physics is described by the Dirac Hamiltonian (2.9) with the Dirac mass (2.13). We call them general honeycomb systems. Examples are monolayer antiferromagnetic manganese chalcogenophosphates (MnPX_3 , $\text{X} = \text{S, Se}$)⁵¹ and perovskite G-type antiferromagnetic insulators grown along [111] direction⁵².

In what follows we analyze the Dirac Hamiltonian (2.9) with the Dirac mass (2.13). It can be positive, negative or zero. The band gap is given by $2|\Delta_s^\eta|$.

III. TOPOLOGICAL PHASE TRANSITION

A. Chern numbers

For any insulating state $|\psi(\mathbf{k})\rangle$ we may define a "gauge potential" in the momentum space by

$$a_k(\mathbf{k}) = -i \langle \psi(\mathbf{k}) | \partial_k | \psi(\mathbf{k}) \rangle, \quad (3.1)$$

which is properly called the Berry connection. Then we may define the "magnetic field" in the momentum space, which is properly called the Berry curvature $F(\mathbf{k})$,

$$F(\mathbf{k}) = \frac{\partial}{\partial k_x} a_y(\mathbf{k}) - \frac{\partial}{\partial k_y} a_x(\mathbf{k}). \quad (3.2)$$

The Chern number is the integral of the Berry curvature $F(\mathbf{k})$ over the first Brillouin zone, which is the total "magnetic flux",

$$\mathcal{C} = \frac{1}{2\pi} \int d^2k F(\mathbf{k}). \quad (3.3)$$

We have calculated the Berry curvature with the use of the tight-binding Hamiltonian (2.8), which we illustrate in Fig.5. The Berry curvature is strictly localized at the K and K' points. This feature remains unchanged even if we include the extra terms (2.14). Consequently, the Dirac Hamiltonian is valid to make a topological analysis to each valley, which is indexed by the spin $s = \uparrow\downarrow$ and the valley index $\eta = \pm$. Namely, it is possible to assign the Chern number \mathcal{C}_s^η to each valley.

When the Hamiltonian is given by (2.9), the Berry curvature is explicitly calculated for each valley as

$$F_s^\eta(\mathbf{k}) = -\eta \frac{\Delta_s^\eta}{2 \left((\hbar v_F k)^2 + (\Delta_s^\eta)^2 \right)^{3/2}}. \quad (3.4)$$

The Chern number is obtained as

$$\mathcal{C}_{s_z}^\eta = -\frac{\eta}{2} \text{sgn}(\Delta_s^\eta), \quad (3.5)$$

where the Dirac mass Δ_s^η is given by (2.13).

The Chern number is quantized as $\mathcal{C}_s^\eta = \pm \frac{1}{2}$. It is insensitive to a deformation of the band structure provided the gap is open. On the other hand, it changes its sign as the Dirac mass Δ_s^η changes its sign. Such a quantity is a topological charge. Hence an insulator phase is indexed by a set of four Chern numbers \mathcal{C}_s^η . A topological phase transition occurs when the sign of the Dirac mass Δ_s^η changes.

It is instructive to make a reinterpretation of the Chern number^{8,9,53}. When the Hamiltonian is given in terms of the 2×2 Hamiltonian as in (2.9), or $H_s^\eta = \boldsymbol{\tau} \cdot \mathbf{d}$ with $d_x = \eta \hbar v_F k_x$, $d_y = \hbar v_F k_y$, $d_z = \Delta_s^\eta$, the Chern number \mathcal{C}_s^η is equivalent to the Pontryagin number,

$$\mathcal{C}_s^\eta = \frac{1}{4\pi} \int d^2k \left(\frac{\partial \hat{\mathbf{d}}}{\partial k_x} \times \frac{\partial \hat{\mathbf{d}}}{\partial k_y} \right) \cdot \hat{\mathbf{d}}. \quad (3.6)$$

The Pontryagin number is a topological number which counts what times the vector $\hat{\mathbf{d}}$ wraps a sphere. We use the polar coordinate of the $\hat{\mathbf{d}}$ vector, $\hat{d}_x \pm i \hat{d}_y = \sqrt{1 - \sigma^2(k)} e^{i\eta\theta}$, $\hat{d}_z = \sigma(k)$, and we obtain

$$\mathcal{C}_s^\eta = \frac{\eta}{4\pi} \int d^2k \varepsilon_{ij} \partial_i \sigma \partial_j \theta = -\frac{\eta}{2} \int_0^1 d\sigma, \quad (3.7)$$

which agrees with (3.5). The pseudospin texture forms a meron structure in the momentum space. A meron is a topological structure which has a half integer Pontryagin number as shown in Fig.6.

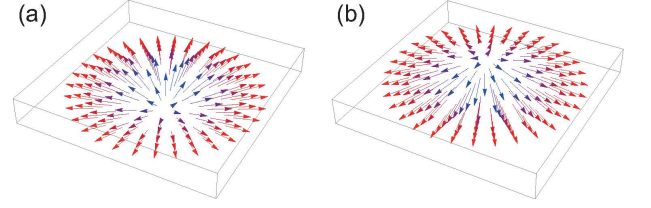


FIG. 6: Illustration of a meron structure in momentum space. A meron with the Pontryagin number (a) $1/2$, which core spin is pointing up direction, (b) $-1/2$, which core spin is pointing down direction.

B. Classification of topological insulators

We have defined four Chern numbers $\mathcal{C}_{s_z}^\eta$. Equivalently we may define the total Chern number \mathcal{C} , the spin Chern number \mathcal{C}_s ^{54–57}, the valley Chern number^{58–60} and the spin-valley Chern number^{58,61},

$$\mathcal{C} = \mathcal{C}_\uparrow^K + \mathcal{C}_\uparrow^{K'} + \mathcal{C}_\downarrow^K + \mathcal{C}_\downarrow^{K'}, \quad (3.8)$$

$$\mathcal{C}_s = \frac{1}{2} (\mathcal{C}_\uparrow^K + \mathcal{C}_\uparrow^{K'} - \mathcal{C}_\downarrow^K - \mathcal{C}_\downarrow^{K'}), \quad (3.9)$$

$$\mathcal{C}_v = \mathcal{C}_\uparrow^K - \mathcal{C}_\uparrow^{K'} + \mathcal{C}_\downarrow^K - \mathcal{C}_\downarrow^{K'}, \quad (3.10)$$

$$\mathcal{C}_{sv} = \frac{1}{2} (\mathcal{C}_\uparrow^K - \mathcal{C}_\uparrow^{K'} - \mathcal{C}_\downarrow^K + \mathcal{C}_\downarrow^{K'}). \quad (3.11)$$

We make an important comment. The valley Chern number and the spin-valley Chern number are well defined only in the Dirac theory. Namely they are ill defined in the tight-binding model. Hence, we may call \mathcal{C} and \mathcal{C}_s the genuine Chern numbers.

Possible sets of genuine Chern numbers $(\mathcal{C}, \mathcal{C}_s)$ are $(0, 0)$, $(2, 0)$, $(0, 1)$, $(1, \frac{1}{2})$ up to the sign \pm . They are the trivial, quantum anomalous Hall (QAH), quantum spin Hall (QSH), spin-polarized quantum anomalous Hall (SQAH) insulators, respectively. Note that there are two-types of trivial band insulators, which are quantum valley Hall (QVH) insulator^{62,63}, and quantum spin-valley Hall (QSVH) insulator with antiferromagnetic (AF) order⁴⁷.

We comment on the relation between the \mathbb{Z}_2 index and the spin Chern number. The spin Chern number \mathcal{C}_s is identical to the \mathbb{Z}_2 index by modulo 2 when there exists the time-reversal symmetry⁵⁴. The spin Chern number is well defined even when there is no time-reversal symmetry, while the \mathbb{Z}_2 index is well defined even when s_z is not a good quantum number.

IV. TOPOLOGICAL EDGE

A. Bulk-edge correspondence

The most convenient way to determine if the system is topological or trivial is to employ the bulk-edge correspondence. When there are two topological distinct phases, a topological phase transition must occur between them. It is generally accepted that the band gap must close at the topological phase transition point since the topological number cannot change

	C_{\uparrow}^K	$C_{\uparrow}^{K'}$	C_{\downarrow}^K	$C_{\downarrow}^{K'}$	C	$2C_s$	C_v	$2C_{sv}$
QAH	1/2	1/2	1/2	1/2	2	0	0	0
SQAH	1/2	1/2	1/2	-1/2	1	1	1	-1
SQAH	1/2	1/2	-1/2	1/2	1	-1	1	1
QVH	1/2	1/2	-1/2	-1/2	0	0	2	0
SQAH	1/2	-1/2	1/2	1/2	1	1	-1	1
QSH	1/2	-1/2	1/2	-1/2	0	2	0	0
QSVH	1/2	-1/2	-1/2	1/2	0	0	0	2
SQAH	1/2	-1/2	-1/2	-1/2	-1	1	1	1
SQAH	-1/2	1/2	1/2	1/2	1	-1	-1	-1
QSVH	-1/2	1/2	1/2	-1/2	0	0	0	-2
QSH	-1/2	1/2	-1/2	1/2	0	-2	0	0
SQAH	-1/2	1/2	-1/2	-1/2	-1	-1	1	-1
QVH	-1/2	-1/2	1/2	1/2	0	0	-2	0
SQAH	-1/2	-1/2	1/2	-1/2	-1	1	-1	-1
SQAH	-1/2	-1/2	-1/2	1/2	-1	-1	-1	1
QAH	-1/2	-1/2	-1/2	-1/2	-2	0	0	0

TABLE II: Corresponding to the spin and valley degrees of freedom, there are 4 Chern numbers $C_{s_z}^\eta$, each of which takes $\pm \frac{1}{2}$. Equivalently they are given by the Chern, spin Chern, valley Chern and spin-valley Chern numbers C , C_s , C_v and C_{sv} . They are independently controlled by the four parameters λ_{SO} , λ_V , λ_Ω and λ_{SX} . Hence there are 16 states indexed by them. The genuine topological numbers are only C and C_s .

its quantized value without gap closing. Note that the topological number is only defined in the gapped system and remains unchanged for any adiabatic process.

To reveal the emergence of gapless modes at a phase transition point, it is convenient to analyze the energy spectrum of a nanoribbon in a topological phase, because the boundary of the nanoribbon separates a topological state and the vacuum whose topological numbers are zero. Indeed, we have pointed out the emergence of gapless edge modes in silicene: See Fig.3(b3). We may call it a topological edge when it separates two topologically distinctive states.

B. Helical edges and Chiral edges

We analyze the edge modes of silicene in detail when silicene is in the QSH phase. The quantum numbers of the edge modes are not clear in Fig.3(b3) since they are degenerate. We may resolve the degeneracy by applying weak electric field E_z to a nanoribbon with zigzag edges as in Fig.7(a). It is an intriguing feature of a zigzag nanoribbon that one of the edges is composed of A sites while the other of B sites. Hence the edge modes occurring in the A sites have higher energy than those in the B sites. This property enable us to identify the edge modes occurring in the upper or lower edges. Second, the spin degeneracy is resolved due to the SO interaction. We have shown up(down)-spin band in magenta(cyan) in Fig.7(a1). Third, the velocity of electrons within the edge

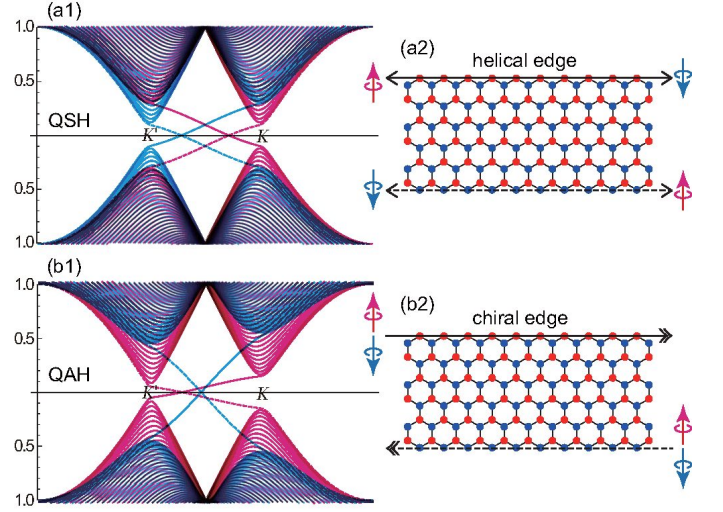


FIG. 7: (a1) Nanoribbon in QSH phase. There are helical edges. We have applied E_z to differentiate the upper (A sites) and lower (B sites) edges, which results in the splitting of the helical edges. (a2) Illustration of helical edge states. Up and down spins flow into the opposite directions. (b1) Nanoribbon in QAH phase. There are chiral edges. (b2) Illustration of chiral edge states. Up and down spins flow into the same directions.

mode is identified by the slope of the band gap. In this way we know how the edge current flows in Fig.7(a2). A prominent feature is the up and down spins flow into the opposite directions along each edge, implying that the edge current is a pure spin current. Such an edge is called a helical edge.

We may also analyze a silicene nanoribbon in the QAH phase. The band structure is given by Fig.7(b1), where we have applied weak electric field E_z to resolve the degeneracy. The spin and the current direction are shown in both edges in Fig.7(b2). The edge current does not convey spins. Such an edge is called a chiral edge.

C. Inner edges

When a nanoribbon has only the valley Chern number and the spin-valley Chern number, no edge modes emerge because these numbers are not defined in the vacuum. Nevertheless these numbers are also topological numbers within the bulk.

We may consider a junction separating two different topological phases in a single honeycomb system¹⁵. We call such a junction an inner edge. In contrast we may call a real edge of a nanoribbon an outer edge. There is a crucial difference between gapless edge modes appearing along an inner edge and an outer edge. Any gapped state is indexed by a set of four topological numbers (C, C_s, C_v, C_{sv}) . Consequently, an inner edge state carries a gapless edge mode indexed by the difference $(\Delta C, \Delta C_s, \Delta C_v, \Delta C_{sv})$ between the two adjacent gapped states. More precisely, we set $\Delta C = C^L - C^R$ and so on, when the topological insulator with $(C^L, C_s^L, C_v^L, C_{sv}^L)$ is on the left-hand side of the one with $(C^R, C_s^R, C_v^R, C_{sv}^R)$. On the other hand, an outer edge state can carry a gapless edge

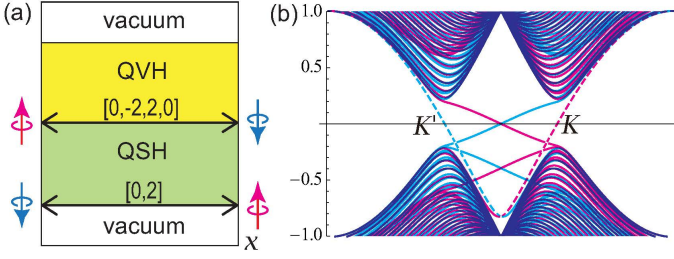


FIG. 8: (a) Silicene nanoribbon placed parallel to the x axis. When external field E_z is applied along the y axis, the region with $E_z > E_{cr}$ becomes a QVH insulator. The inner edge between the QSH and QVH parts is helical. The outer edge below the QSH part is also helical. No gapless edge states appear along the outer edge above the QVH part. (b) The band structure of a silicene nanoribbon. Four gapless edge modes are found, which are assigned as in (a).

mode only indexed by $(\mathcal{C}, \mathcal{C}_s)$ of the gapped state because the valley Chern numbers are ill defined in the vacuum.

We illustrate a nanoribbon which contains the QSH and QVH phases in Fig.8, where there are two outer edges and one inner edge. As we have argued, the outer edge of the QSH part is helical, while the outer edge of the QVH part has no gapless edge modes. The nature of the inner edge is seen by analyzing the band structure in Fig.8(b). It contains only four nondegenerate gapless states. On one hand, two solid lines correspond to the helical edge between the QSH part and the vacuum. On the other hand, two dotted lines correspond to the inner edge between the QSH and QVH parts, which is also helical. It should be noted that the inner edge modes cross the Fermi energy at the K and K' points.

D. Topological Kirchhoff law

We consider a configuration where three different topological insulators meet at one point: See Fig.9. In this configuration there are three edges forming a Y-junction. The condition which edges can make a Y-junction is the conservation of these topological numbers at the junction. This law is a reminiscence of the Kirchhoff law, which dictates the conservation of currents at the junction of electronic circuits. We call it the topological Kirchhoff law⁶¹.

We present an interesting interpretation of the topological Kirchhoff law. We may regard each topological edge state as a world line of a particle carrying the four topological charges. The Y-junction may be interpreted as a scattering process of these particles. In this scattering process, the topological charges conserve. We have shown that we can control the mass of Dirac cones with the spin and valley independently in silicene. Our findings will open a new way to topological spin-valleytronics, where the spin and valley degrees of freedom and the topology are fully manipulated.

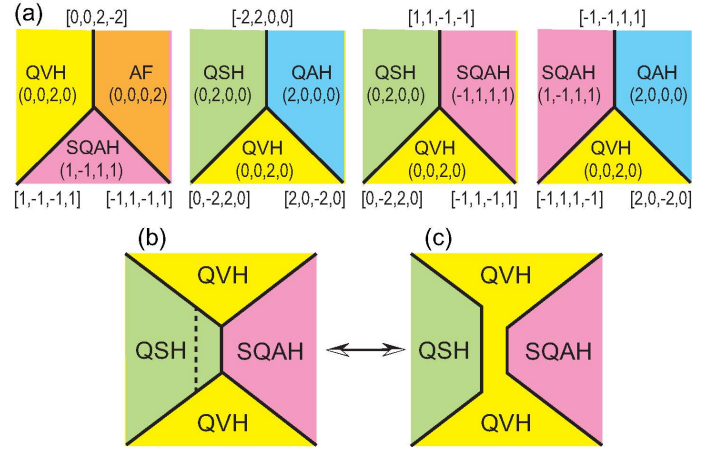


FIG. 9: (a) Y junctions of topological edge currents, which are made of the boundaries of three different topological insulators. (b) and (c) Topological circuits made of topological edges. We apply electric field to the center region of the QSH phase in (b). The region, to which electric field is applied, becomes a QVH phase. As a result, the connected edge states are separated as shown in (c).

V. GAPLESS EDGE MODE IN DIRAC THEORY

We construct the Dirac theory of a gapless inner-edge state^{15,61} indexed by η and s . It emerges along a curve where the Dirac mass vanishes, $\Delta_s^\eta(x, y) = 0$.

A. Rectangular geometry

We take the edge along the x axis. Zero modes emerge along the line determined by $\Delta_s^\eta(y) = 0$. We may set $k_x = \text{constant}$ due to the translational invariance along the x axis. The equation of motion $H_K \psi = 0$ reads

$$(-i\hbar v_F \tau_y \partial_y + \Delta_s^\eta \tau_z) \psi = 0. \quad (5.1)$$

We set $\psi_B = i\zeta \psi_A$ with $\zeta = \pm 1$, and seek the zero-energy solution. Here, ψ_A is a two-component amplitude with up and down spins, $\psi_A = (\psi_A^\uparrow, \psi_A^\downarrow)$. Furthermore, setting $\psi_A(x, y) = e^{ik_x x} \phi_A(y)$, we obtain $H_\eta \psi_A(x, y) = E_{\eta\zeta} \psi_A(x, y)$ together with $E_{\eta\zeta} = \eta\zeta \hbar v_F k_x$, and

$$(\xi \hbar v_F \partial_y - \Delta_s^\eta(y)) \phi_A(y) = 0. \quad (5.2)$$

By solving this, the zero-energy solution is given by

$$\psi_A(x, y) = C e^{ik_x x} \exp \left[\frac{\zeta}{\hbar v_F} \int^y \Delta_s^\eta(y') dy' \right], \quad (5.3)$$

and $\psi_B(x, y) = i\zeta \psi_A(x, y)$, where C is the normalization constant. The sign of $\zeta = \pm 1$ is determined so as to make the wave function finite in the limit $|y| \rightarrow \infty$. This is a reminiscence of the Jackiw-Rebbi mode⁶⁴ presented for the chiral mode. The difference is the presence of the spin and valley indices in the wave function.

B. Circular geometry

We consider a cylindrical symmetric domain with the radius r_0 at the origin of the xy plane. A phase transition occurs at $r = r_0$, where $\Delta_s^\eta(r) = 0$. The equation of motion $H_K \psi = 0$ reads

$$\begin{aligned} \Delta_s^\eta(r) \psi_{s,A}^\eta + \hbar v_F e^{i\eta\theta} \left(i\partial_r - \frac{1}{r} \partial_\theta \right) \psi_{s,B}^\eta &= 0, \\ \hbar v_F e^{-i\eta\theta} \left(i\partial_r + \frac{1}{r} \partial_\theta \right) \psi_{s,A}^\eta - \Delta_s^\eta(r) \psi_{s,B}^\eta &= 0. \end{aligned} \quad (5.4)$$

We can solve this for zero-energy states as

$$\psi_{s,A}^\eta(r, \theta) = \frac{C}{\sqrt{r}} e^{i\eta\theta/2} \exp \left[\frac{\xi}{\hbar v_F} \int_0^r \Delta_s^\eta(r') dr' \right], \quad (5.5)$$

and $\psi_B(r, \theta) = i\zeta \psi_A(r, \theta)$, where C is the normalization constant and $\zeta = \pm 1$. The sign of ζ is determined so as to make the wave function finite in the limit $r \rightarrow \infty$.

C. Interface induced by electric field

We apply an inhomogeneous electric field,

$$\Delta_s^\eta(r) = \lambda_{SO} - \lambda_V(r) \quad (5.6)$$

with $\lambda_V(r) = \ell E_z(r) > \lambda_{SO}$ for $r < r_0$. The region $r < r_0$ is a trivial insulator, while the region $r > r_0$ is a quantum spin-Hall insulator. The zero-energy helical edge current flows along the circle $r = r_0$.

VI. TOPOLOGICAL QUANTUM FIELD-EFFECT TRANSISTOR

We next calculate the conductance of a nanoribbon by using the Landauer formalism^{65,66}. The conductance is quantized in silicene nanoribbons. Indeed, one channel has a quantized conductance e^2/h . Accordingly, the conductance is obtained by counting the number of bands. We show the conductance in Fig.10. When electric field is not applied, there are helical edge states, which contribute to the conductance $2e^2/h$ since up and down spin channels contribute to the conductance. When the electric field E_z exceeds the critical value E_{cr} , the edge states disappear since the nanoribbon becomes a trivial insulator, which results in zero conductance. This means the system acts as a transistor where the "on" state can be switched to the "off" state by applying electric field. This transistor is "quantum" since the conductance is quantized, which is highly contrasted with the ordinal transistor, where the conductance is not quantized. Furthermore the conductance is topologically protected because the zero-energy edge state is topologically protected. Namely the conductance is robust against impurities due to its topological stability. Consequently we may call it a field-effect topological quantum transistor⁶⁶. This is the most energy-saving device since it utilizes the minimum conductance.

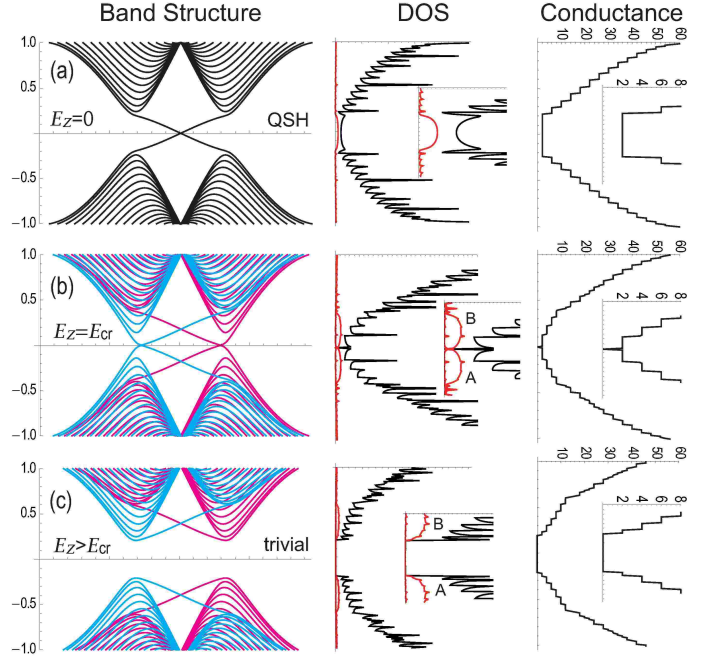


FIG. 10: (Color online) Band structure, DOS and conductance of zigzag silicene nanoribbons for (a) the QSH insulator phase, (b) the metallic phase at the phase transition point, and (c) the trivial insulator phase. These phases are obtained by applying electric field E_z . The phase transition occurs at $E_z = E_{cr}$. The number of bands is $2W + 2$ in the nanoribbon with width W . Here, the width is taken to be $W = 31$, and only a part of bands are shown. The band gap is degenerate (nongenerate) with respect to the up (red) and down (blue) spins at $E_z = 0$ ($E_z > 0$). Van Hove singularities emerge in the DOS at the points where the band dispersion is flat. The site-resolved DOS of the up-spin state at the outmost A and B sites of a nanoribbon are shown by red curves in the insets. There are finite DOS for the zero-energy edge states in the QSH insulator. The conductance is quantized by unit of e^2/h .

We have calculated the density of states (DOS) $\rho(E)$ and the conductance $\sigma(E)$ of a nanoribbon as functions of the Fermi energy E , which is controlled by doping. We give the results at electric field $E_z = 0, E_{cr}$ and $2E_{cr}$ in Fig.10. A van Hove singularity occurs in the DOS at the point where the band dispersion is flat. As E increases beyond the point, the Fermi level crosses a new band. A new channel opens and contributes to the conductance by e^2/h for each spin and valley. It is clearly observed that the edge channel connects the tips of the Dirac cones with the same spin at the K and K' points.

We have also plotted the site-resolved DOS $\rho_i(E)$ of the up-spin states at the outmost A and B sites of a nanoribbon by red curves in the insets [Fig.10]. They represent degenerate zero-energy states at $E_z = 0$. As we have explained in Fig.7, the energy of the A and B sites become different for $E_z \neq 0$. It results in the downward (upward) shift of $\rho_{A(B)}(E)$ along the edge as E_z increases. They are separated completely, and zero-energy states disappear for $E_z > E_{cr}$.

VII. QUANTUM ANOMALOUS HALL EFFECTS

Silicene has an additional interaction term, which we have so far neglected. It is the Rashba SO interaction given by

$$-i\frac{2}{3}\lambda_R \sum_{\langle\langle i,j \rangle\rangle_{\alpha\beta}} \mu_i c_{i\alpha}^\dagger \left(\boldsymbol{\sigma} \times \hat{\mathbf{d}}_{ij} \right)_{\alpha\beta}^z c_{j\beta} \quad (7.1)$$

in the tight-binding model. Here, λ_R represents the Rashba SO coupling strength associated with next-nearest neighbor hopping, where $\mu_i = \pm 1$ for the A (B) site, and $\hat{\mathbf{d}}_{ij} = \mathbf{d}_{ij}/|\mathbf{d}_{ij}|$ with the vector \mathbf{d}_{ij} connecting two sites i and j in the same sublattice⁴⁶. The Dirac theory of the Rashba term is given by

$$\eta\tau_z a\lambda_R (k_y\sigma_x - k_x\sigma_y). \quad (7.2)$$

The Rashba term vanishes at the K and K' points. Hence the Rashba interaction is negligible as far as the low-energy physics near the Dirac points is concerned.

There exists an exceptional case in which we cannot neglect the Rashba interaction. We have previously studied the interaction term (2.13) affecting the Dirac mass. There is another type of interactions, which do not contribute to the Dirac mass but shift the bands into the opposite directions between up and down spins. The most important one is given by the exchange interaction,

$$M \sum_{is} s c_{is}^\dagger c_{is} \quad \text{or} \quad M\sigma_z \quad (7.3)$$

in the tight-binding model or in the Dirac theory. We show the band structure of a nanoribbon with the exchange interaction in Fig.11(a). We see that the two Dirac cones with the opposite spins approach as $|M|$ increases and touch each other at $|M| = \lambda_{SO}$. Then, we expect naively the level crossing to occur for $|M| > \lambda_{SO}$, that is, the two Dirac cones to penetrate into each other. Actually, the level crossing turns into the level anticrossing due to the spin mixing caused by the Rashba interaction λ_R . The new phase is the QAH insulator⁶⁷ with the Chern number 2. We show the Berry curvature in Fig.11(b), where it takes a large value where the bands almost touch the Fermi energy away from the K and K' points. The spin direction is inverted and the spin forms a skyrmion texture, which results in the Chern number 1. The total Chern number is 2 since there are two skyrmions at the K and K' points.

VIII. SYMMETRY PROTECTED TOPOLOGICAL CHARGE

The Chern number \mathcal{C} is always quantized. However, the other ones \mathcal{C}_i are not so when the relevant symmetry is broken. Indeed, the spin s_z symmetry is broken by the Rashba interaction. We here analyze this problem.

There exists an alternative expression for the Chern number in terms of the Green function⁶⁸. It reads

$$\mathcal{C} = \frac{\varepsilon_{\alpha\beta\gamma}}{6} \int \frac{d^2k}{(2\pi)^2} \int_{-\infty}^{\infty} d\omega \times \text{Tr}[G\partial_{k_\alpha} G^{-1} G\partial_{k_\beta} G^{-1} G\partial_{k_\gamma} G^{-1}], \quad (8.1)$$

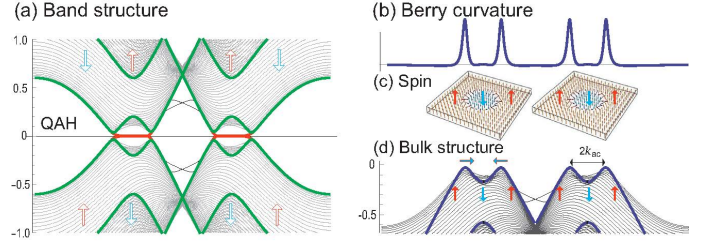


FIG. 11: (a) The energy spectrum of a QAH state. Gray curves are for a nanoribbon. Heavy green curves represent the energy spectrum of the bulk, calculated independently. A gap opens in the bulk spectrum, where almost flat gapless modes appear at the edges of a nanoribbon. A red (blue) arrow indicates the spin direction away from the Fermi level. (b) (a) Berry curvature, (b) spin, and (c) band structure of a QAH state calculated based the Dirac theory. Gray curves represent the energy spectrum of a nanoribbon. Spins rotate by the Rashba interaction near the Fermi level, generating a skyrmion spin texture in the momentum space. It generates a non-trivial Berry curvature along the anticrossing circle. The integration of the Berry curvature gives the Chern number $\mathcal{C} = 2$, since there are two skyrmions each of which yields $\mathcal{C} = 1$.

where k_α , k_β and k_γ run through $k_0 \equiv i\omega$, k_x and k_y , while $G(\omega, \mathbf{k})$ is the Matsubara Green's function,

$$G(\mathbf{k}) = \frac{1}{i\omega - H(\mathbf{k})}, \quad (8.2)$$

with $i\omega$ referring to the Matsubara frequency (ω : real). This formula has a merit that it can be used even in the presence of interactions^{69–71}.

We propose to define the following quantities⁷²,

$$\tilde{\mathcal{C}}_i = \frac{\varepsilon_{\alpha\beta\gamma}}{6} \int \frac{d^2k}{(2\pi)^2} \int_{-\infty}^{\infty} d\omega \times \text{Tr}[\chi_i G\partial_{k_\alpha} G^{-1} G\partial_{k_\beta} G^{-1} G\partial_{k_\gamma} G^{-1}], \quad (8.3)$$

for $i = s, v, sv$ together with $\chi_s = \sigma_z$, $\chi_v = \eta_z$, $\chi_{sv} = \sigma_z\eta_z$. Provided the spin σ_z and the pseudospin η_z are good quantum numbers, namely, $[H, \sigma_z] = [H, \eta_z] = 0$, we are able to prove that these are identical to (3.9), (3.10) and (3.11) by following the method⁷³. We may use the formula (8.3) even if symmetries are broken. They are no longer quantized when the symmetries are broken. Accordingly, we call them symmetry protected topological charges.

In the presence of the Rashba interaction, the spin Chern number is explicitly calculated as

$$\tilde{\mathcal{C}}_s = \frac{\mathcal{C}_s}{[1 + (a\lambda_R/\hbar v_F)^2]},$$

where \mathcal{C}_s is the spin Chern number without the Rashba interaction. This yields $\tilde{\mathcal{C}}_s = 1 - 5.9 \times 10^{-7}$, where we have used $v_F = 5.5 \times 10^5$ m/s, $a = 3.86 \text{ \AA}$ and $\lambda_{R2} = 0.7$ meV as sample parameters of silicene. Surely $\tilde{\mathcal{C}}_s$ is not quantized, but the deviation is negligibly small. Furthermore, we can check that the edge mode remains practically gapless. The spin mixing can be neglected in practical purposes.

IX. TOPOLOGICAL SUPERCONDUCTOR

Topological superconductors are superconductors which have nontrivial topological numbers^{8,9}. The bulk band spectrum has a full gap due to the superconducting gap, while the edge states appear at the sample of edges as in the case of topological insulators. An intriguing feature is that these edge states support Majorana fermions^{74,75}.

A. Majorana fermion

Majorana fermion is one of the hottest topics in the condensed matter physics. Majorana fermion operator γ satisfies the anti-commutation relation $\{\gamma, \gamma^\dagger\} = 1$ and the Majorana condition $\gamma = \gamma^\dagger$, indicating that a Majorana fermion is a particle which is its own anti-particle.

In the BCS theory, superconductor is expressed by the Bogoliubov–de Gennes (BdG) Hamiltonian,

$$H = \frac{1}{2} \sum_k \begin{pmatrix} c_k^\dagger & c_{-k} \end{pmatrix} H_{\text{BdG}}(k) \begin{pmatrix} c_k \\ c_{-k}^\dagger \end{pmatrix}, \quad (9.1)$$

based on the Nambu representation (c_k, c_{-k}^\dagger) , which is a combination of the particle and hole operators. The BdG Hamiltonian has a particle-hole symmetry,

$$\Xi H_{\text{BdG}} \Xi^{-1} = -H_{\text{BdG}}, \quad (9.2)$$

with respect to the particle-hole operator Ξ satisfying $\Xi^2 = 1$. The states with the energy E and $-E$ are to be identified in the Nambu representation. The creation and annihilation operators of these two states satisfy $\gamma_E^\dagger = \gamma_{-E}$. Consequently, we obtain $\gamma_0^\dagger = \gamma_0$ for a single zero-energy state ($E = 0$) if there is such one. As a result, a single zero-energy state with the particle-hole symmetry is a Majorana fermion.

B. Topological superconductor in honeycomb system

A topological superconductor is obtained from a QAH insulator by attaching an s -wave superconductor to it⁷⁶. Indeed, Cooper pairs are formed between up and down spins at the same site of the honeycomb system. The resultant BCS Hamiltonian reads $H_{\text{BCS}} = H_K + H_{K'} + H_{\text{SC}}$ with

$$\begin{aligned} \hat{H}_{\text{SC}} = & \sum_{\tau=A,B} [\Delta_{\text{SC}} c_{\tau\uparrow}^{K\dagger}(k) c_{\tau\downarrow}^{K'\dagger}(-k) + \Delta_{\text{SC}} c_{\tau\uparrow}^{K'\dagger}(k) c_{\tau\downarrow}^{K\dagger}(-k)] \\ & + \text{h.c.} \end{aligned} \quad (9.3)$$

in the momentum representation, where Δ_{SC} is the superconducting gap. A finite gap present in a superconducting state allows us to evaluate the Chern number of the state to determine whether it is topological. Alternatively we may examine the emergence of gapless edge modes by calculating the band structure of a nanoribbon with zigzag edge geometry based on

this Hamiltonian. The BCS Hamiltonian is rewritten into the BdG Hamiltonian,

$$H_{\text{BdG}} = \begin{pmatrix} H_K(k) & H_\Delta \\ H_\Delta^\dagger & -H_{K'}^*(-k) \end{pmatrix}, \quad (9.4)$$

by introducing the Nambu representation for the basis vector, i.e., $\Psi = \{\psi_{A\uparrow}^K, \psi_{B\uparrow}^K, \psi_{A\downarrow}^K, \psi_{B\downarrow}^K, \psi_{A\uparrow}^{K'\dagger}, \psi_{B\uparrow}^{K'\dagger}, \psi_{A\downarrow}^{K'\dagger}, \psi_{B\downarrow}^{K'\dagger}\}^t$.

Diagonalizing the BdG Hamiltonian, we obtain the energy spectrum. It consists of eight levels with the eigenvalues

$$E_{\text{BdG}}^{\alpha,\beta}(k) = \pm \sqrt{(\hbar v_F k)^2 + (E_0^{\alpha,\beta})^2} \quad (9.5)$$

with

$$E_0^{\alpha,\beta} = \sqrt{((\lambda_{\text{SO}} - \alpha\lambda_V)^2 + \Delta_{\text{SC}}^2)} + \beta(\lambda_{\text{H}} + \alpha\lambda_{\text{SX}}), \quad (9.6)$$

where α and β takes ± 1 . The gap closes ($E_0^{\alpha,\beta} = 0$) at

$$(\lambda_{\text{H}} + \alpha\lambda_{\text{SX}})^2 = (\lambda_{\text{SO}} - \alpha\lambda_V)^2 + \Delta_{\text{SC}}^2. \quad (9.7)$$

Though the original Hamiltonian is an 8×8 matrix, we may decompose it into 4 independent 2×2 Hamiltonians,

$$H^{\alpha,\beta}(k) = \begin{pmatrix} \beta E_0^{\alpha,\beta} & \hbar v_F k_- \\ \hbar v_F k_+ & -\beta E_0^{\alpha,\beta} \end{pmatrix}, \quad (9.8)$$

corresponding to $\alpha, \beta = \pm 1$. This Hamiltonian reproduces the energy spectrum (9.5). We may interpret $\beta E_0^{\alpha,\beta}$ as the modified Dirac mass due to the BCS condensation.

It is straightforward to calculate the Chern number of the superconducting honeycomb system H_{BdG} . It is determined by the sign of the modified Dirac mass⁵³,

$$C = \frac{1}{2} \sum_{\alpha,\beta=\pm 1} \text{sgn}(\beta E_0^{\alpha,\beta}). \quad (9.9)$$

The condition of the emergence of a topological superconductivity is $C \neq 0$. Note that it is zero when the time-reversal symmetry is present. In order to obtain a non-zero Chern number, λ_{SX} or λ_{H} must be nonzero. It should be noticed that the spin Chern number is no longer defined due to the BCS condensation of the up-spin and down-spin electrons. The topological phase diagram is easily constructed in the $(\lambda_{\text{SO}}, \lambda_V, \lambda_{\text{SX}}, \lambda_{\text{H}}, \Delta_{\text{SC}})$ space. The phase boundaries are given by (9.7). The Chern number is determined from (9.9).

C. Majorana fermion in honeycomb system

We consider a disk region in a honeycomb sheet, as illustrated in Fig.12. We may tune parameters λ_{SO} , λ_V , λ_{SX} , λ_{H} and Δ_{SC} to become space-dependent so that the inner region has a different Chern number from the outer region. There appears gapless edge modes at the phase boundary, where $E_0^{\alpha,\beta}(r) = 0$. According to a general theorem, as we have

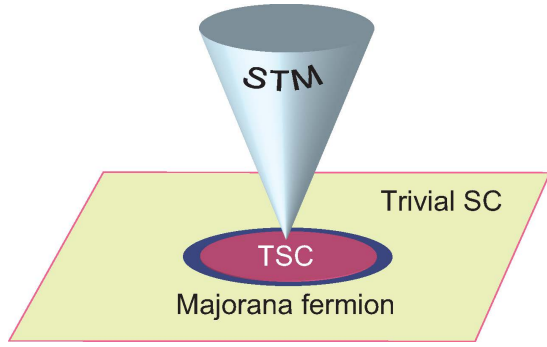


FIG. 12: Illustration of a Majorana zero-energy state between two topological phases. By applying electric field E_z locally, we may create a topological spot ($C = 1$) in a trivial superconductor ($C = 0$). There appears a zero-energy Majorana state at the phase boundary.

reviewed, a zero-energy state with the particle-hole symmetry is always a Majorana fermion.

There are several ways to make $E_0^{\alpha,\beta}(r_c) = 0$, since there are four independent mass parameters λ_{SO} , λ_V , λ_{SX} , λ_H and one superconducting gap Δ_{SC} . A simple way is to keep only one parameter and Δ_{SC} . We consider the case where electric field is applied to a disk region of an antiferromagnetic topological superconductor ($\lambda_{SX} \neq 0$), as shown in Fig.12. Very strong electric field can be applied experimentally by an STM probe. We assume electric field is strong enough so that

$$\lambda_V(r) = \ell E_z(r) = \pm \lambda_{SO} + \sqrt{\lambda_{SX}^2 - \Delta_{SC}^2}. \quad (9.10)$$

The critical field is of the order of $E_z^{cl} = 0.1V\text{\AA}^{-1}$. The inner region of the circle have a nontrivial Chern number $C = 1$ and becomes a topological superconductor. On the other hands, the outer region of the disk have $C = 0$ and remains to be the trivial superconductor. As a result, there emerges one Majorana fermion localized at the boundary of the circle. Its wave function is given by (5.5).

- ¹ A.H. Castro Neto, F. Guinea, N.M.R. Peres, K.S. Novoselov and A.K. Geim, Rev. Mod. Phys. **81** 109 (2009).
- ² S. Das Sarma, S. Adam, E. H. Hwang, and E. Rossi, Rev. Mod. Phys. **83**, 407 (2011).
- ³ M. O. Goerbig, Rev. Mod. Phys. **83**, 1193 (2011).
- ⁴ V. N. Kotov, B. Uchoa, V. M. Pereira, F. Guinea, and A. H. Castro Neto, Rev. Mod. Phys. **84**, 1067 (2012).
- ⁵ M. I. Katsnelson, Graphene: Carbon in Two Dimensions (Cambridge Univ. Press, Cambridge, 2012).
- ⁶ Gian G. Guzmán-Verri and L. C. Lew Yan Voon, Phys. Rev. B **76** (2007) 075131.
- ⁷ Y. Xu, B. Yan, H.-J. Zhang, J. Wang, G. Xu, P. Tang, W. Duan, and S.-C. Zhang, Phys. Rev. Lett. **111**, 136804 (2013).
- ⁸ M.Z Hasan and C. Kane, Rev. Mod. Phys. **82**, 3045 (2010).
- ⁹ X.-L. Qi and S.-C. Zhang, Rev. Mod. Phys. **83**, 1057 (2011).
- ¹⁰ K. Takeda and K. Shiraishi, Phys. Rev. B **50** (1994) 075131.
- ¹¹ S. Cahangirov, M. Topsakal, E. Akturk, H. Sahin, and S. Ciraci, Phys. Rev. Lett. **102**, 236804 (2009).
- ¹² S. Lebegue and O. Eriksson, Phys. Rev. B **79**, 115409 (2009).
- ¹³ N. D. Drummond, V. Zolyomi, V. I. Fal'ko, Phys. Rev. B **85**, 075423 (2012).
- ¹⁴ Z. Ni, Q. Liu, K. Tang, J. Zheng, J. Zhou, R. Qin, Z. Gao, D. Yu and J. Lu, Nano Lett. **12** 113 (2012)
- ¹⁵ M. Ezawa, New J. Phys. **14**, 033003 (2012).
- ¹⁶ Z.-X. Guo, S. Furuya, J. Iwata, A. Oshiyama, J. Phys.Soc. Jpn. **82**, 063714 (2013); Phys.Rev. B **87**, 235435 (2013)
- ¹⁷ B. Lalmi, H. Oughaddou, H. Enriquez, A. Kara, S. Vizzini, B. Ealet, and B. Aufray, Appl. Phys. Lett. **97** (2010) 223109.
- ¹⁸ P.E. Padova, C. Quaresima, C. Ottaviani, P.M. Sheverdyaeva, P. Moras, C. Carbone, D. Topwal, B. Olivieri, A. Kara, H. Oughaddou, B. Aufray, and G.L. Lay, Appl. Phys. Lett. **96** (2010) 261905.
- ¹⁹ B. Aufray A. Vizzini, H. Oughaddou, C. Lndri, B. Ealet, and G.L. Lay, Appl. Phys. Lett. **96** (2010) 183102.
- ²⁰ P. Vogt, P. De Padova, C. Quaresima, J. Avila, E. Frantzeskakis, M. C. Asensio, A. Resta, B. Ealet and G. Le Lay Phys. Rev. Lett. **108**, 155501 (2012)
- ²¹ C.-L. Lin, R. Arafune, K. Kawahara, N. Tsukahara, E. Minamitani, Y. Kim, N. Takagi and M. Kawai, Appl. Phys. Express **5** 045802 (2012)
- ²² B. Feng, Z. Ding, S. Meng, Y. Yao, X. He, P. Cheng, L. Chen, and K. Wu, Nano Lett. **12** 3507 (2012)
- ²³ A. Fleurence, R. Friedlein, T. Ozaki, H. Kawai, Y. Wang, and Y. Yamada-Takamura, Phys. Rev. Lett. **108**, 245501
- ²⁴ L. Meng, Y. Wang, L. Zhang, S. Du, R. Wu, L. Li, Y. Zhang, G. Li, H. Zhou, W. A. Hofer and H.-J. Gao, Nano Lett., **13** 685 (2013)
- ²⁵ D. Chiappe, E. Scalise, E. Cinquanta, C. Grazianetti, B. van den Broek, M. Fanciulli, M. Houssa and A. Molle, Adv. Mat. **26** 2096 (2014)
- ²⁶ M. E. Davila, L. Xian, S. Cahangirov, A. Rubio and G. Le Lay, New. J. Phys. **16** 095002 (2014).
- ²⁷ L. Li, S.-Z. Lu, J. Pan, Z. Qin, Y.-Q. Wang, Y. Wang, G.-Y. Cao, S. Du and H.-J. Gao, Adv. Mat. **26** 4820 (2014).
- ²⁸ C.-L. Lin, R. Arafune, K. Kawahara, M. Kanno, N. Tsukahara, E. Minamitani, Y. Kim, M. Kawai, and N. Takagi, Phys. Rev. Lett. **110**, 076801 (2013).
- ²⁹ Y. Fukaya, I. Mochizuki, M. Maekawa, K. Wada, T. Hyodo, I. Matsuda, and A. Kawasuso, Phys. Rev. B **88**, 205413 (2013)
- ³⁰ L. Chen, B. Feng and K. Wu, Appl. Phys. Lett **102**, 081602 (2013)
- ³¹ E. Noguchi, K. Sugawara, R. Yaokawa, T. Hitosugi, H. Nakano and T. Takahashi, Adv. Mat. **27** 856 (2015).
- ³² Paola De Padova,^{1,a} P. Vogt, A. Resta, J. Avila, I. Razado-Colambo, C. Quaresima, C. Ottaviani, B. Olivieri, T. Bruhn, T. Hirahara, T. Shirai, S. Hasegawa, M. C. Asensio, and G. Le Lay, Appl. Phys. Lett. **102**, 163106 (2013)
- ³³ L. Tao, E. Cinquanta, D. Chiappe, C. Grazianetti, M. Fanciulli, M. Dubey, A. Molle and D. Akinwande, Nat. Nanotech. **10**, 227–231 (2015)
- ³⁴ A. Kara, H. Enriquez, A. P. Seitsonen, L.C. L. Y. Voon, S. Vizzini, B. Aufray, H. Oughaddou, Surface Science Reports **67**, 1 (2012)
- ³⁵ Q. Tang, Z. Zhou, Progress in Materials Science **58** 1244 (2013)
- ³⁶ Y. Yamada-Takamura and R. Friedlein, Sci. Technol. Adv. Mater. **15** 064404 (2014)
- ³⁷ Y. Cai, C.-P. Chuu, C. M. Wei and M. Y. Chou, Phys. Rev. B **88**, 245408 (2013).

- ³⁸ T. P. Kaloni, M. Tahir, U. Schwingenschlogl, *Sci. Rep.* **3**, 3192 (2013).
- ³⁹ S. Kokott, L. Matthes and F. Bechstedt, *physica status solidi (RRL)* **7** 538 (2013)
- ⁴⁰ S. Kokott, P. Pflugradt, L. Matthes and F. Bechstedt, *J. Phys. Condens. Matter* **26** 185002 (2014)
- ⁴¹ S. Sattar, R. Hoffmann, U. Schwingenschl, *New J. Phys.* **16**, 065001 (2014)
- ⁴² M. Neek-Amal, A. Sadeghi, G. R. Berdiyrov, F. M. Peeters, *Appl. Phys. Lett.* **103**, 261904 (2013)
- ⁴³ R. Quhe, Y. Yuan, J. Zheng, Y. Wang, Z. Ni, J. Shi, D. Yu, J. Yang, and J. Lu, *Sci. Rep.* **4** 5476 (2014)
- ⁴⁴ C.-C. Liu, W. Feng, and Y. Yao, *Phys. Rev. Lett.* **107** (2011) 076802
- ⁴⁵ C. L. Kane and E. J. Mele, *Phys. Rev. Lett.* **95**, 226801 (2005); *ibid* **95**, 146802 (2005).
- ⁴⁶ C.-C. Liu, H. Jiang, and Y. Yao, *Phys. Rev. B*, **84** (2011) 195430.
- ⁴⁷ M. Ezawa, *Phys. Rev. B* **87**, 155415 (2013)
- ⁴⁸ T. Oka and H. Aoki, *Phys. Rev. B* **79**, 081406(R) (2009).
- ⁴⁹ T. Kitagawa, T. Oka, A. Brataas, L. Fu, and E. Demler, *Phys. Rev. B* **84**, 235108 (2011).
- ⁵⁰ M. Ezawa, *Phys. Rev. Lett.* **110**, 026603 (2013)
- ⁵¹ X. Li, T. Cao, Q. Niu, J. Shi, and J. Feng, *PNAS* **110** 3738 (2013)
- ⁵² Q.-F. Liang, L.-H. Wu, X. Hu, *New J. Phys.* **15** 063031 (2013)
- ⁵³ M. Ezawa, *Eur. Phys. J. B* **85**, 363 (2012).
- ⁵⁴ E. Prodan, *Phys. Rev. B* **80**, 125327 (2009); *New J. Phys.* **12**, 065003 (2010).
- ⁵⁵ D. N. Sheng, Z. Y. Weng, L. Sheng and F. D. M. Haldane, *Phys. Rev. Lett.* **97** 036808 (2006).
- ⁵⁶ Y. Yang, Z. Xu, L. Sheng, B. Wang, D.Y. Xing, and D. N. Sheng, *Phys. Rev. Lett.* **107**, 066602 (2011).
- ⁵⁷ L. Sheng, D. N. Sheng, C. S. Ting, and F. D. M. Haldane, *Phys. Rev. Lett.* **95**, 136602 (2005).
- ⁵⁸ F. Zhang, J. Jung, G. A. Fiete, Q. Niu and A. H. MacDonald, *Phys. Rev. Lett.* **106**, 156801 (2011)
- ⁵⁹ F. Zhang, A. H. MacDonald, and E. J. Mele, *Proc. Natl. Acad. Sci. USA* **110**, 10546 (2013).
- ⁶⁰ J. Li, A. F. Morpurgo, M. Büttiker, and I. Martin, *Phys. Rev. B* **82**, 245404 (2010).
- ⁶¹ M. Ezawa, *Phys. Rev. B* **88**, 161406 (R) (2013)
- ⁶² W.-K. Tse, Z. Qiao, Y. Yao, A. H. MacDonald, Q. Niu, *Phys. Rev. B* **83**, 155447 (2011).
- ⁶³ Z. Qiao, H. Jiang, X. Li, Y. Yao, and Q. Niu, *Phys. Rev. B* **85**, 115439 (2012).
- ⁶⁴ R. Jackiw and C. Rebbi, *Phys. Rev. D* **13**, 3398 (1976).
- ⁶⁵ S. Datta, *Electronic Transport in Mesoscopic Systems* (Cambridge University Press, Cambridge, England, 1995); *Quantum Transport: Atom to Transistor* (Cambridge University Press, England, 2005)
- ⁶⁶ M. Ezawa, *Appl. Phys. Lett.* **102**, 172103 (2013)
- ⁶⁷ M. Ezawa, *Phys. Rev. Lett* **109**, 055502 (2012)
- ⁶⁸ G. E. Volovik, *The Universe in a Helium Droplet* (Oxford University Press, New York, 2003).
- ⁶⁹ Z. Wang, X.-L. Qi, and S.-C. Zhang, *Phys. Rev. Lett.* **105**, 256803 (2010)
- ⁷⁰ Z. Wang and S.-C. Zhang, *Phys. Rev. X* **2**, 031008 (2012).
- ⁷¹ V. Gurarie, *Phys. Rev. B* **83**, 085426 (2011).
- ⁷² M. Ezawa, *Phys. Lett. A*, **378**, 1180 (2014).
- ⁷³ X.-L. Qi, T. Hughes, S.-C. Zhang, *Phys. Rev. B* **78** 195424 (2008).
- ⁷⁴ J. Alicea, *Rep. Prog. Phys.* **75**, 076501 (2012).
- ⁷⁵ C.W.J. Beenakker, *Annu. Rev. Con. Mat. Phys.* **4**, 113 (2013)
- ⁷⁶ X.-L. Qi, T. L. Hughes, and S.-C. Zhang, *Phys. Rev. B* **82**, 184516 (2010).